Lattice-Boltzmann simulations of active fracture model parameter for tilted channel networks

Hakan Başağaoğlu [*], Sauro Succi, Chandrika Manepally,
Randall Fedors, Danielle Y. Wyrick

Abstract: A two-dimensional multiphase lattice-Boltzmann model was implemented to analyze the sensitivity of the active fracture model parameter (Liu et al., 1998) to fracture network orientation and injection scenarios in a partially saturated, variably dipping, and geometrically simple fracture network. The numerical experiments were conducted for continuous and intermittent injections from a single port and continuous injections from multiple ports. The results indicated that the active fraction of a fracture network that contributes to fracture flow was sensitive to fracture network orientation, injection rate, injection mode, and flow regimes. The active fraction of fractures differed by as much as ~20% when these factors were included in the simulations. Although the active fracture parameter is used as a fitting parameter in continuum-based models for field-scale unsaturated flow and transport problems, the numerical results suggest the linkage to fracture network orientation and flow regimes should be explored to strengthen its technical basis and range of applicability.

1. Introduction

The active fracture model, AFM (Liu et al., 1998), was proposed to account for the reduction in the number of fracture channels and fracture-matrix interfacial area in flow and transport simulations for unsaturated fractured rocks. Only some of the fractures in a fracture network participate in unsaturated flow, and only a portion of those fracture surfaces may exhibit flowing water. The motive for the AFM was based on experimental and field evidence that only a small portion of connected fractures may contribute to flow and transport across the unsaturated fractured domain at Yucca Mountain, Nevada (Liu and Bodvarsson, 2001; Liu et al., 2003, 2004; Seol et al., 2003; Zhou et al., 2006). Observations at other sites and in laboratory experiments support the reduction in fracture–matrix interaction area (Su et al., 1999; Wood et al., 2004; Mathias et al., 2005). Rivulet or finger flow at lower flow rates is an illustrative example for the reduction in the fracture-matrix interaction area.

The AFM is applicable to gravity-dominated, nonequilibrium, and preferential liquid water flow in fracture channels different from capillary equilibrium-based flow models because capillary strength in fracture networks is relatively less significant than in porous

H. Basagaoglu, C. Manepally, Center for Nuclear Waste Regulatory Analyses, Southwest Research Institute, San Antonio, TX 78238 USA; S. Succi, Istituto Applicazioni Calcolo, CNR-IAC Viale del Policlinico 137, 00161, Rome, Italy; R. Fedors, US Nuclear Regulatory Commission, MS T-7F27, Washington, D.C. 20555 USA; D. Wyrick, Department of Earth, Material, and Planetary Sciences, Southwest Research Institute, San Antonio, TX 78238 USA. [*]Corresponding author (hbasagaoglu@swri.org).

media (Zhou et al., 2002). In the AFM, the active fraction of fractures, f_a (the ratio of the number of fractures that contribute to fracture flows to the total number of fractures), is assumed to be a power function of the effective fracture saturation in connected fractures, S_e (Liu et al., 1998):

$$f_a = S_e^\gamma,$$ (1)

where γ is the active fracture parameter, which is considered to be a fitting parameter in continuum–based models ($\gamma \le 1$). The effective water saturation is defined as $S_e = (S_f - S_r)/(1 - S_r)$, in which S_f is the water saturation in connected fractures and S_r is the residual water saturation. All dry fractures are presumed to be at the residual water saturation. With this construction, the total fracture-matrix interface area, A_{fm}, defined over the entire unsaturated flow domain, is reduced to an active fracture-matrix interface area, A'_{fm}, the active fraction of fracture walls contacted by water. The reduction in the interface area was given (Liu et al., 1998):

$$\frac{A'_{fm}}{A_{fm}} \cong S_e^{1-\gamma}$$ (2)

Eq. 2 was built on the premise that the walls of active fractures were represented by parallel plates and mobile water exists in connected, locally saturated fracture segments. This equation indicates that if the entire fracture network is fully saturated, $S_e \to 1$, then $A'_{fm} \to A_{fm}$ and $\gamma \to 1$ for a well-posed problem. The concept of the AFM is supported by, in particular, seepage data analyses from field tests, and the γ has been used as a calibration parameter, describing fingering flow in fracture networks in a number of large scale numerical analyses of flow and transport simulations (Liu and Bodvarsson, 2001; Liu et al., 2003, 2004; Seol et al., 2003; Zhou et al., 2006). It was also implemented in deriving an analytical solution for solute transport in an unsaturated single fracture-matrix system to account for possible reductions in fracture-matrix contact areas (Houseworth, 2006). The AFM parameter was calibrated by comparing numerical solutions using a two-dimensional discrete-fracture-network model and a one-dimensional dual-continuum model in simulating flow and transport in a 1 m^3–sized fractured rock block (Seol et al., 2006). The authors noted that γ did not fully capture the complexity of the fractured flow at the scale of their experiment.

Fracture data from the Topopah Spring Tuff (geologic unit for the proposed waste emplacement drifts) in the Exploratory Studies Facility and the Enhanced Characterization of the Repository Block cross-drift at Yucca Mountain has been characterized by the U.S. Department of Energy (Albin et al., 1997; Mongano et al., 1999; Nieder-Westermann, 2000) and reanalyzed by Smart et al. (2006). The analyses reveal that most fractures are either gently dipping (dip angles less than 20%) or steeply dipping (dip angles greater than 70%). In continuum-based numerical models built on constitutive relations, γ has been commonly treated as a property of a fracture network

and used as a calibration parameter without explicitly relating it to fracture network orientation and flow regime. At the field scale, the flow regime is a function of percolation rate and fracture characteristics (e.g., Ghezzehei, 2004). In the following work, the main focus is to investigate the sensitivity of γ to the orientation of a geometrically simple fracture network under (i) continuous injection of water from a single port, (ii) continuous injection of water from multiple injection ports, and (iii) intermittent injection of water at fixed time intervals from a single injection port. The correlations between γ obtained from different fracture counting schemes and the effective saturations are explored. The results are useful for strengthening the technical basis and applicability of the active fracture model for simulating field scale flow and transport in slanted and partially saturated fracture channel networks. We considered different modeling approaches for the numerical experiments and chose to use a multiphase lattice-Boltzmann model due to its computational efficiency, ease of handling irregular boundaries, contact angle dynamics, and ease of extending the analyses to three dimensions using real fracture data for future studies.

2. Lattice–Boltzmann (LB) Method

In LB models, the fluid is represented as an ensemble of particles that synchronously stream along the bonds of a regular lattice and undergo mass- and momentum-conserving collisions at the nodes (Benzi et al., 1992; Wolf-Gadrow, 2000; Succi, 2001). The microdynamics of the LB model with a single relaxation time (BGK) model (Bhatnagar et al., 1954) are described by:

$$f_k\left(\mathbf{x}+\mathbf{e}_k\,\Delta t, t+\Delta t\right)-f_k\left(\mathbf{x},t\right)=\frac{f_k^{eq}\left(\mathbf{x},t\right)-f_k\left(\mathbf{x},t\right)}{\tau}, \tag{3}$$

where $f_k\left(\mathbf{x},t\right)$ is the population density at the lattice node at position $\mathbf{x}$ at time t along the velocity vector $\mathbf{e}_k$, f_k^{eq} is the equilibrium Maxwell-Boltzmann distribution function, τ is the relaxation parameter, and Δt is the time increment. A two-dimensional nine-velocity (D2Q9) model was used in this study. The discrete velocity vector basis for the D2Q9 model consists of the null vector, four vectors of length unity directed toward the nearest neighbor nodes, and four vectors of length $\sqrt{2}$ directed toward the next-nearest neighbor nodes. The discrete equilibrium Maxwell-Boltzmann distribution is approximated by the low-Mach number mass- and momentum-conserving expansion (Qian et al., 1992):

$$f_k^{eq}=\omega_k\rho\left(1+\frac{\mathbf{e}_k\cdot\mathbf{u}}{c_s^2}+\frac{\left(\mathbf{e}_k\cdot\mathbf{u}\right)^2}{2c_s^4}+\frac{\mathbf{u}\cdot\mathbf{u}}{2c_s^2}\right), \tag{4}$$

where ω_k is the weight coefficient for the kth vector (4/9 for the null vector, 1/9 for the nearest neighbor vectors, and 1/36 for the next-nearest neighbor vectors). The local macroscopic density and velocity at a lattice site can be computed from the distribution

functions at that site as $\rho = \sum_{k=0}^{8} f_k$ and $\rho \mathbf{u} = \sum_{k=0}^{8} f_k \mathbf{e}_k$. With the equilibrium distribution in Eq. 4, the Navier-Stokes equations can be recovered through a Chapman-Enskog expansion, which indicates that the kinematic viscosity of the fluid is $\nu = c_s^2 (\tau - 0.5)$, and the sound velocity is $c_s = 1/\sqrt{3}$ in lattice units.

First-order phase separation processes can be simulated by modifying the net momentum at the lattice sites by incorporating the effects of density-dependent fluid-fluid interaction forces that involve only neighboring nodes separated by a distance of $|e_k|$ (when $\Delta t = 1$). The resulting rate of momentum change at each lattice site for a two-phase system (Shan and Chen, 1993; 1994) is given by:

$$\frac{d\mathbf{P}}{dt} = -\psi(\mathbf{x}) \sum_{k=0}^{8} (\omega_k G_f \psi(\mathbf{x} + \mathbf{e}_k)(1 - s(\mathbf{x} + \mathbf{e}_k)) + G_s s(\mathbf{x} + \mathbf{e}_k)) \mathbf{e}_k, \tag{5}$$

where $\psi(\mathbf{x})$ is a function of the density at the lattice node at position $\mathbf{x}$, G_f is the fluid-fluid interaction strength, G_s is the solid-fluid interaction strength, and $s(.)$ is 0 for a fluid or 1 for a solid node. When the flow is driven by gravity, the momentum, $\rho \mathbf{u}$, at each lattice node is replaced by $\rho \mathbf{u} + \tau (d\mathbf{P}/dt + \rho \mathbf{g})$. With the interaction potential in Eq. 5, the total momentum at each site is not conserved locally, but the total momentum is conserved globally. In our simulations, we chose the form $\psi(\mathbf{x}) = 1 - e^{-\rho(x)}$ and $\Delta x / \Delta x = 1$. A bounce-back scheme (Benzi et al., 1992; Wolf-Gadrow, 2000; Succi, 2001) was used to simulate no-slip behavior along the boundaries of the flow domain.

Macroscopic equations governing the motion of each component in the Shan-Chen model have been derived (Shan and Doolen, 1995) using the Chapman-Enskog method (Chapman and Cowling, 1960). Through the Chapman-Enskog expansion (by Taylor-expanding Eq. 3 in the Knudsen number, $\varepsilon \sim (\Delta x \nabla M)/M$, where M is any macroscopic field), it can be shown that pressure, p, in equation of state, $p(\rho) = c_s^2 (\rho + G_f (\psi(\rho))^2 / 2)$, satisfies the momentum-balance equation, $\partial \mathbf{u}/\partial t + (\mathbf{u} \cdot \nabla)\mathbf{u} = -\nabla p/\rho$ (Shan and Doolen, 1995). The approach used to derive the second-order momentum equation (that accounts for the shear stress, $\nu \nabla^2 \mathbf{u}$) for a single phase fluid (by Taylor-expanding Eq. 3 in ε^2) without interparticle interactions can be applied to a single component two-phase system by noting that the fluid-fluid interaction forces between nearest lattice nodes, $-c_s^2 G_f \psi(\rho) \nabla \psi(\rho)$, do not affect the shear viscosity, at least to second order (Shan and Doolen, 1995). When the first- and second-order momentum equations are added, the equation $\partial \mathbf{u}/\partial t + (\mathbf{u} \cdot \nabla)\mathbf{u} = -\nabla p/\rho + \nu \nabla^2 \mathbf{u}$ can be recovered, given that $\nabla \cdot \mathbf{u} \sim 0$.

The Shan-Chen (SC) model is based on the use of pseudopotentials that depend on space and time only through the density field, rather than atomistic potentials, as is appropriate for a mesoscopic model. Despite such a drastic simplification, the model captures two essential ingredients of nonideal fluids: a nonideal equation of state and interfacial

tension. This simplification is appropriate for analyzing properties that do not depend on atomistic details nor on the specific form of the equation of state (Sbragaglia et al., 2006; Benzi et al., 2006a, 2006b). It has been recently shown that the LB model with the SC potentials provides realistic simulations and information about the flow behavior even beyond the strictly hydrodynamic regime, $\varepsilon \rightarrow 0$ (Basagaoglu et al., 2007), consistent with similar observations in Toschi and Succi (2005) and Sbragaglia and Succi (2006). Moreover, the LB models are suitable for simulating flow in complex flow geometries (Succi et al., 1989) and avoids problems such as interface broadening and grid entanglement.

A one-component two-phase formulation of the SC model has been used to simulate bubble growth on, and detachment from, horizontal and vertical surfaces (Sehgal et al., 1999) to study two-phase flow in a two-dimensional homogeneous and regularly packed synthetic porous system (Yang et al., 2001) and to simulate interfacial configurations in partially saturated porous media (Sukop and Or, 2004). The LB model with the SC interaction potential was used to simulate flow in unsaturated flow systems (Pan et al., 2004; Sukop and Or, 2004). Although the SC model was incapable of handling high density contrasts such as 1:1000 (and hence it may hinder the complete dimensional analysis based on actual values of system parameters), the flow characteristics in partially saturated flow domains were reasonably well captured in these studies.

New multiphase LB models with large density contrasts have been formulated (Inamuro et al., 2004; Lee and Lin, 2005; Zheng et al., 2006), although they have not yet been validated with the pore-scale experimental data for flow and transport in unsaturated porous and fractured flow domains. Thus, an agreement on the general flow characteristics obtained from LB simulations and the recently reported experiment of Huang et al. (2005), along with their two-dimensional numerical results (based on the Volume of Fluid method, (VOF)) was explored a priori to assess the performance of the LB model with SC potentials in simulating partially saturated flow in a slanted fracture network.

3. Simulations involving a single injection port

A flow experiment using a geometrically simple fabricated fracture network that consists of horizontal and vertical flow channels with uniform aperture was reported by Huang et al. (2005). The representation of the fracture network used in their flow experiment is shown in Fig. 1a. We counted fracture channels in two different schemes in this study. In the first counting scheme (CS1), the flow domain has a total of 19 flow channels consisting of 5 long horizontal and 14 short vertical channels (Fig. 1b). Alternatively, fracture channels on either side of fracture junctions were numbered separately (CS2), which resulted in a total of 42 flow channels (Fig. 1c). Water was injected at an injection port close to the left side of the topmost vertical channel at a constant rate while the apparatus was kept tilted $2.5°$ counterclockwise. The top boundary of the flow domain was a no-flow boundary except at the fracture. The lateral boundaries were impermeable, and a free drainage condition was imposed at the bottom.

Huang et al. (2005) provided a numerical simulation of fluid flow across the smooth-walled fracture network using a two-dimensional VOF method. They noted a qualitative agreement, especially in the lower portions of the flow domain, between the VOF simulation and the flow experiment considering the flow modes, penetration depth and quasi-steady behavior of the fluid. They attributed the discrepancies between the experiment and simulations to the two-dimensional nature of the simulation and possible spatial variations in surface roughness that might have affected both spatial aperture and contact angle dynamics. In this study, agreement between the simulation results of Huang et al. (2005) and the results from the dimensionless LB simulation was sought, specifically focusing on the flow modes and the resultant quasi-steady flow paths. If the general flow characteristics from two-dimensional VOF simulation results of Huang et al. (2005) are captured equally well with the two-dimensional multiphase LB model, then the LB simulation can be used to study general flow characteristics within the partially saturated fracture channel network.

In the flow experiment of Huang et al. (2005), the apparatus was tilted by $2.5°$; hence, gravitational forces have components g'_x and g'_y in horizontal and vertical directions, respectively. For the LB model, new gravitational strengths for the tilted fracture network were determined using $g'_y = g_y \cos\theta$ and $\tan\theta = g'_x/g'_y$, in which g_y is the vertical component of the gravitational strength for a tilting angle of $0°$. An injection rate, q_{inj}, on the order of $10^{-3} \Delta t \sqrt{g'^2_x + g'^2_y}$ was used in the LB simulations to be consistent with the experiment (in the experiment, $g = 9.81$ m/s^2, the volumetric flow rate, Q_{inj}, was $2.5 \cdot 10^{-7}$ m^3/s, and q_{inj} was ~0.02 m/s).

The flow patterns from a LB simulation at early, intermediate, and late stages are shown in Fig. 2. The flow modes, penetration depths, and quasi-steady flow paths are in good agreement with three snapshots obtained by the VOF simulations in Fig. 3(d-f) of Huang et al. (2005). Based on visual inspection, both model results are identical in simulating (i) one-sided wetting of vertical fracture walls, (ii) gradual backfilling of the leftmost portion of the third horizontal channel from the top, (iii) preferential filling channels on the left side of the network, and (iv) penetration depths of the invading fluid across the channel network. Hence, the essential flow characteristics observed in the flow experiment were captured equally well by the LB and VOF simulations. Moreover, the comparison of model results suggest that a density contrast of ~70, a computational limit with the SC model (corresponding to G_f = -6.5 in Eq. 5 (Basagaoglu et al., 2004)) in multiphase LB simulations, was large enough to capture the general flow characteristics successfully.

Next, the LB model was used to explore the sensitivity of the active fracture parameter, γ, to the orientation of the fracture (channel) network used in the experiment for single and multiple continuous and single intermittent injection scenarios. The model was also used to explore the proper fracture counting scheme (Fig. 1b-c) best representing the active fracture parameter. Because the LB simulation was initially compared to two-dimensional VOF simulations of Huang et al. (2005), the remaining LB simulations were

carried out in two dimensions. In our numerical experiments, the tilting angle of the apparatus varied between $0° - 45°$.

Fig. 3 shows the flow patterns and the penetration depth of water when the injected water reached the lower boundary, and Fig. 4 shows the total elapsed time for quasi-steady saturations for different network orientations, θ, respectively. In general, the fractured domain reached quasi-steady saturations at earlier times as the apparatus was tilted more. However, at moderate tilting angles (e.g., $13°$), the steady-state saturations were achieved at relatively longer times due to more frequent flow fragmentation and coalescence of fluid drops around the solid zones (Fig. 3e). The active fracture parameter, γ, was computed using effective saturations in the active fractures as the water reached the exit-end of the flow domain (Case 1) and quasi-steady water saturations in the fracture network (Case 2). The Case 1 was simulated because multiphase flows in natural settings are rarely at a steady-state (saturations computed from Case 1 were within 3–28% of the quasi-steady saturations). Because simulations ended as the injected water reached the lower end of the flow domain in Case 1, the volume of injected water differed in each simulation with different tilt angles, which affected the saturation of the fractured medium at the end of the simulation. However, the volume of injected water was the same at all tilt angles for Case 2.

Fig. 3 shows that flow in fractures was more dispersed at low tilt angles, and more focused at high tilt angles, indicating the sensitivity of flow focusing to the fracture network orientation. At all tilting angles, the leftmost portion of the third horizontal channel (from the top) was filled up where the fluid encountered highest flow resistance due to a sudden blockage to the flow path and an immediate flow path change to the right. At high tilting angles, the order and portion of the filled horizontal channels on the leftmost side of the fractured domain varied with the tilt angle. This is crucial for fracture systems with heterogeneous fracture-matrix interfaces because the location of the mass transfer (and hence the resultant volume and mass-exchange rate) is strongly determined by the fracture network orientation. For example, if the dissolved phase mass transfer rate at the fracture–matrix interface was significant only at the upper leftmost portion of the first two horizontal channels from the top, then there would not be any significant mass transfer between the fracture and matrix for tilt angles $<13°$. Fig. 3 also shows that flow in the lower portions of the fracture network exhibited flow path switches in conjunction with film flow on channel walls and flow fragmentation and coalescence around impermeable solid zones especially at intermediate tilt angles.

The final saturation profile of the invading wetting fluid (water), S_f, and the normalized solid-fluid interface length (or area with a unit depth), A'_{fm}/A_{fm}, is shown as a function of the tilting angle, θ, in Fig. 5 at the time the invading fluid reached the exit-end of the flow domain and at the quasi-state saturations. Fig. 5 reveals that both S_f and A'_{fm}/A_{fm} are sensitive to the fracture network orientation for $\theta < 20°$ for Case 1 and $\theta < 15°$ for Case 2 (the effect of lateral boundaries was important for $\theta > 20°$ for Case 1 and for $\theta > 15°$ for Case 2). At low tilting angles $\left(\theta \le 2.5°\right)$, the wetting fluid had a

longer time to spread across the domain, which led to a longer solid-fluid interface length and higher saturations. At intermediate tilting angles $\left(10° \leq \theta \leq 15°\right)$, the tilting angle decreased the arrival time of the invading fluid (first arrival time for $\theta = 13°$ was 0.57 times shorter than for $\theta = 0°$) and reduced its spread, resulting in less saturation, more focused flow, and smaller solid-fluid interface length. At larger tilting angles ($\theta \geq 20°$ for Case 1 and $\theta \geq 20°$ for Case 2), the variations in S_f and A'_{fm}/A_{fm} with respect to the tilting angle were relatively small (the saturation of the invading fluid strongly correlated with the normalized solid-fluid interface length at different tilting angles (with a correlation coefficient of 0.98). Both the water saturation and normalized solid-fluid interface length, determined when the injected water reached the lower boundary, were at the minimum values when the apparatus was slanted $12.5°$. However, the minimum values were observed at $11°$ when the simulations continued until the quasi-steady saturations (within 1% for all cases) were reached. But the sensitivity of the normalized interfacial length and saturations to the fracture network orientation did not change significantly when the simulation ended as the injected water reached the lower boundary (with different injected water volumes at different tilt angles) or continued until the steady-state saturations were reached (with the same injected water volume at different tilt angles). The maximum difference in saturations and the normalized solid-fluid interface lengths at different tilting angles were as much as 0.15–0.17 and 0.17–0.20, respectively, revealing the significant effects of fracture network orientation on the water saturation and solid-fluid interface length.

4. Determining the active fracture parameter

Solid-fluid interface length (or area with a unit depth) is obtained directly from numerical simulations, and the active fracture parameter, γ, can be computed from Eq. 2 as a function of a fracture network orientation and the residual saturation, S_r. The resultant equation becomes, $\gamma = 1 - \left(\log\left(A'_{fm}/A_{fm}\right)\right)/\log S_e$. The relation between γ and the tilting angle, θ, for $S_r = 0.04$ and $S_r = 0.08$ is shown in Fig. 6 (these residual saturation levels were arbitrarily chosen). The AFM parameter, γ, varied with the tilting angle in the range of 0.11–0.17 for $S_r = 0.04$ and 0.20–0.28 for $S_r = 0.08$, when the injected water reached the lower free-drainage boundary. At the quasi–steady limits, γ ranged from 0.11 to 0.16 for $S_r = 0.04$ and from 0.20 to 0.26 for $S_r = 0.08$, indicating that the use of quasi-steady water saturations instead of water saturations when the injected water reached the lower boundary of the flow domain had a small effect on γ.

5. Determining the active fraction of fractures

Once the AFM parameter, γ, is obtained as a function of the fracture network orientation, f_a, the active fraction of fractures can be determined from Eq. 1. The results (Fig. 7a) indicate that the minimum active fraction of fractures was obtained at $13°$ (corresponding to the highest γ) at different residual saturation levels, S_r. The active fraction of

fractures were relatively more sensitive to the tilting angle at low S_r. As S_r was reduced by half, the active fraction of fractures decreased by 20%, indicating equal importance of S_r and the fracture network orientation (the active fraction of fractures for $0°$ and $13°$ differs by 23% for $S_r = 0.08$). The results at the quasi-steady saturation (Fig. 7b) are consistent with these results, except that the minimum number of active fractures was obtained at a tilting angle of $\theta = 11°$ for $S_r = 0.04$ and $\theta = 13.5°$ for $S_r = 0.08$. Independent of whether the simulation continued until the quasi-steady saturations were reached or ended when the water reached the lower drainage boundary, the number of active fractures had a minimum value at $11° \leq \theta \leq 13.5°$. Based on these numerical results, the numerical experiments described in the subsequent sections continued until the injected fluid reached the lower boundary of the fracture network.

The active fracture model parameter, γ, computed in Fig. 6 from S_e and A'_{fm} using Eq. 2 for $S_r = 0.04$ and 0.08 was compared against the γ obtained by counting the number of wet fractures based on two different fracture counting schemes in Fig. 1(b-c). Fig. 8 shows that γ, as a function of the tilting angle, calculated from the two fracture counting schemes, was weakly correlated with γ in Fig. 6a. However, it was correlated slightly better with γ from the counting scheme in Fig. 1c than in Fig. 1b. Thus, for the fractured domain studied herein, γ can be viewed as a qualitative measure that accounts for relative changes in the active fraction of fractures that contributes to fracture flows and may not necessarily provide the active fraction of fractures precisely. However, such a qualitative measure for active fractures is still useful at field scale problems, because the exact geometry of fractures and their spatial connectivity are often not available in real-world systems.

6. Simulations involving multiple injection ports

Water was continuously injected into the channel network from equally spaced multiple injection ports (a total of 2, 4, and 8) located in the uppermost vertical channel at an equal rate simultaneously (Fig. 9). The total volume of water injected into the fracture network at a given time was directly proportional to the number of injection ports. Hence, the volumetric rate of the injected water was determined by the number of active ports. The main objective was to test the performance of the active fracture model at different water injection rates for different fracture network orientations. As expected, water saturation across the flow domain increased as more injection ports were activated. In this case, the issues to be investigated are (a) the possibility of a distinct minimum water saturation and active interface length with respect to the fracture network orientation at large water saturations, as was the case with a single injection port in Fig. 5; (b) sensitivity of the range of γ, as a function of fracture network orientation, to different water saturation levels induced by different water injection rates; and (c) the ability of the active fracture parameter to capture the likelihood of a relatively higher fraction of active fractures at higher injection rates.

Simulation results revealed that as more injection ports were utilized (higher volumetric injection rates), the penetration depth and extent of injected water increased throughout the channels (Fig. 9); fracture channels on the left side were invaded more by water because the entire network was tilted to the left by $2.5°$ in this example. The effect of tilting on the spatial distribution of water was more pronounced at lower water saturations. Fig. 10 reveals that as water was injected at higher rates into the flow domain (higher S_e) more fracture channels became active (higher f_a), but the active fraction of fractures that contributes to fracture flows, f_a, became relatively less sensitive to the fracture network orientation. When these results are combined with the results at the quasi–steady saturations discussed in Section 3, the volumetric injection rate is more important than injected water volume in determining the active fracture parameters and the active fraction of fractures for the slanted fracture domain. Moreover, flow convergence is more pronounced at low injection rates than at high injection rates (high flow convergence represents less dispersed flow across a fracture network). The dependence of f_a on the flow rate agrees well with the numerical results using a surrogate fractured domain reported by Seol et al. (2006). This is due to different saturation profiles at different injection rates as shown in Fig. 9.

The active fraction of fractures as a function of the fracture network orientation behaved like a convex function with a distinct local minimum at an intermediate tilting angle when either 1 or 2 injection ports were used. The minimum number of active fractures was obtained at $θ = 13°$ with a single injection port and at $θ = 17.5°$ with two injection ports. When more injection ports were used, the minimum number of active fractures was achieved at larger tilting angles. The range of active fraction of fractures for a single injection port was ~2.3 times larger (0.30 vs. 0.13) than for 8 injection ports, indicating relatively higher sensitivity of f_a to the fracture network orientation at low water saturations than at high saturations. Fig. 10d indicates that the active fraction of fractures for high volumetric rates for the simulations with 8 injection ports when $θ < 17.5°$ and with 4 injection ports when $θ = 5°$ exceeds 1 (1.0–1.08). Such unphysical results suggest that the empirical relations given in Eqs. (1) and (2) may not hold accurately at near full saturations, but these equations still qualitatively capture relative changes in the fraction of active fractures with the injection rates reasonably well.

Based on the numerical results at low injection rates, the active fraction of fractures may be more sensitive to the fracture network orientation in unsaturated rocks, such as at Yucca Mountain, Nevada, where the climate is semiarid and the net infiltration is low (ranging up to several tens of mm per year). Hence, the treatment of subhorizontal and subvertical channels as perfectly horizontal and vertical channels may over or underestimate the active fracture parameters.

7. Simulations involving disrupted injections from a single port

In natural systems, infiltration events into unsaturated systems are often intermittent. To simplify the analysis here, a constant injection rate from a single port was interrupted at

predefined intervals. The injection interval in lattice units was normalized by dividing it by the total simulation length when the water was injected into the system without interruption.

Temporal variations in saturations, S_f, normalized active solid-fluid interface length, A'_{fm}/A_{fm}, active fracture parameter, γ, and the active fraction of fractures, f_a, are shown in Fig. 11. The results indicated that S_f, A'_{fm}/A_{fm}, and f_a behaved like a sinusoidal function, which can be approximately scaled to a function $y(x) = x\cos(2\pi x^\kappa)$ where x is analogous to the injection interval and $\kappa < 1$ is a scale factor for the wavelength. The differences in S_f and A'_{fm}/A_{fm} at different injection intervals were due to different modes of discontinuity and fragmentation of water films (Fig. 12). Because the injection was disrupted at predefined (normalized) time intervals, water films on channel walls displayed discontinuities more often than the cases with uniform and continuous injections. In practice, discontinuities in water films on fracture walls can potentially impede the transport of dissolved phase species and colloidal particles. In the numerical experiment, when the normalized injection interval ranged from 0.04 to 0.98, the active fraction of fractures varied as much as 15%, revealing the sensitivity of the active fraction of fractures to the injection intervals. Hence, based on these numerical results, an estimate for the active fracture parameter based on the assumption of uniform infiltration rate may differ from its actual value, and the significance of the difference would be related to the degree of the sporadic nature of the infiltration events.

8. Discussion and conclusions

A two-dimensional multiphase lattice-Boltzmann (LB) model was used to simulate the recently reported multiphase flow experiment (Huang et al., 2005) accompanied with a two-dimensional numerical solution based on the volume of fluid method (VOF). In the flow experiment, water was injected into a slightly tilted, initially dry, and geometrically simple fracture network that consisted of horizontal and vertical channels with a spatially constant fracture aperture. The numerical results from the two-dimensional LB model and two-dimensional VOF were in good agreement in regards to the flow mode, penetration depth, and the quasi-steady flow paths of the injected water. The multiphase LB model combined with active fracture model of Liu et al. (1998) was used to analyze the dependence of the active fraction of fractures on the fracture network orientation under continuous water injection at a constant rate or intermittent water injection from a single port and water injection from multiple ports with the volume of injected water proportional to the number of activated ports.

The results from simulations with a single injection port indicated that at low saturations, the active fraction of fractures was sensitive to the channel network orientation at low tilting angles up to $15° - 20°$ and resulted in the active fraction of fractures, f_a, differing as much as 12–23% for arbitrarily chosen residual saturations of 0.04 and 0.08, when the tilting angle varied in the range of $0 - 13°$. The effect of lateral boundaries on the flow paths was important at tilt angles greater than $20°$ when the injected water reached the

lower boundary or greater than $15°$ at the quasi-steady saturations. At relatively low water saturations at the end of the simulations driven by the lower water volume injection, f_a became less sensitive to the fracture network orientation at high tilting angles. Using the fracture water saturations when the injected fluid first reached the lower boundary domain or quasi-steady water saturations had small effects on the active fracture parameter at the low injection rate.

The duration of the flow experiment of Huang et al. (2005) was short, and rectangular blocks around the flow channels were impermeable; therefore, there was no fluid exchange between the channels and the solid zones. However, if the solid zones were porous, fluid exchange between fracture and matrix would likely occur across channel surfaces where the invading water contacts solid surfaces. Flow from fracture to the matrix is controlled by the residence time of flowing water in fractures relative to the imbibition rate of the matrix; thus, the fracture flow rate and the matrix saturation and permeability at the interface are important. If rectangular blocks are envisioned as a matrix with very low porosity and matrix permeability at the fracture-matrix interface, then the contact zones of the wetting fluid (water) on solid surfaces would represent a fracture-matrix interface area (with a unit depth) that will change dynamically until the quasi-steady saturation is reached. Even if the matrix was porous and partially saturated in the experiment, the active fraction of the fracture network would likely not change significantly, but the elapsed time for quasi-steady saturations would be relatively longer.

The sensitivity of f_a to the fracture network orientations at low saturations increased at the end of the simulations when less water was injected from a small number of injection ports (one or two), compared to higher saturations with more injection ports used (four or eight). At low injection rates, the relation between f_a and the tilting angle behaved like a convex function with a local minimum at intermediate tilting angles, $\theta = 13.5° - 17.5°$. The relation between f_a and the tilting angles behaved like a (nearly) monotonically decreasing function with the minimum f_a at higher tilting angles. The range of f_a with respect to the tilting angle was ~2 times larger when the injection rate increased eightfold (a single injection port vs. eight injection ports). Comparison of results with single injection at the quasi-steady limit and multiple injections revealed that the volumetric injection rate is more critical than the injected volume for active fracture number calculations. Moreover, flow convergence is more sensitive to fracture network orientation at low injection rates than at high injection rates (injected water spreads less across the fracture network at high flow convergence).

When injection was intermittent, water films on fracture walls displayed discontinuities more frequently than for noninterrupted injection scenarios. When the water was injected from a single injection port and the injection was disrupted at equal time intervals, the resultant f_a varied at different injection intervals as much as ~15% when the fracture network was slanted by $2.5°$. The difference could probably be much larger in three-dimensional flow domains as the fracture connectivity would likely be higher in three dimensions than in two dimensions. Hence, the conclusion drawn from two-dimensional

analyses in this study would provide only qualitative insights into three-dimensional analyses.

In summary, the numerical experiments revealed that the active fracture parameter, γ, and the active fraction of fractures, f_a, displayed variations with the fracture network orientation, injected water volume, water injection modes, and flow regimes. Based on our numerical exercises, the computed f_a could have deviated from the true value by as much as ~20%, when the fracture network orientation, injection rates, and injection modes were not explicitly addressed in the simulations. The active fraction of fractures, f_a, determined by direct counting of active fractures using two different fracture counting schemes did not correlate well with the f_a computed from the AFM. The AFM is an empirical approach that could have some value in continuum-scale flow and transport modeling, but it should be used cautiously when extrapolating outside the range of calibrated observations. In light of results from the numerical experiments in this study, in field scale analyses, the active fracture parameter obtained from small field tests may not represent the active fracture parameter correctly at larger scales if the main fracture orientation and characteristics are scale dependent. Moreover, the active fracture parameter should be used cautiously if the injection (or percolation) rate is highly sporadic in space and time. The AFM parameter should be related to the major fracture network orientation, injection (percolation) rates, and sporadic nature of injections to enhance its technical basis and extend its applicability.

6. Acknowledgment

Units
25.4 mm = 1 inch
0.3048 m = 1 ft
1 ml = 0.061 in^3 or 0.0338 fl oz

7. References

Albin, A.L., W.L. Singleton, T.C. Moyer, A.C. Lee, R.C. Lung, G.L.W. Eatman, and D.L. Barr 1997. Geology of the main drift-station 28+00 to 55+00, exploratory

studies facility, Yucca Mountain project, Yucca Mountain, Nevada. Milestone Report SPG42AM3. LSN #: DEN001438807 Participant #: MOL.19970804.0137. Bureau of Reclamation and U.S. Geological Survey, Denver, CO. (http://www.lsnnet.gov/results.aspx).

Basagaoglu, H., C.T. Green, P. Meakin, and B. J. McCoy 2004. Lattice-Boltzmann simulation of coalescence-driven island coarsening, J. Chem. Phys. 374:7987–7995.

Basagaoglu, H., P. Meakin, S. Succi, and R. Rotondi 2007. Density fluctuations in lattice-Boltzmann simulations of multiphase fluids in a closed system. Physica A 374:691–698.

Bhatnagar, P.L., E.P. Gross, and M. Krook 1954. A model for collision process in gases, I, small amplitude processes in charged and neutral one component systems. Phys. Rev. 94:511–525.

Benzi, R., S. Succi, and M. Vergassola 1992. The lattice Boltzmann equation: Theory and applications. Phys. Rep. 222:145–197.

Benzi, R., L. Biferale, M. Sbragaglia, S. Succi, and F. Toschi 2006a. Mesoscopic two-phase model for describing apparent slip in micro-channel flows. Europhys. Lett. 74: 651–657.

Benzi, R., L. Biferale, M. Sbragaglia, S. Succi, and F. Toschi 2006b. Mesoscopic modeling of a two-phase flow in the presence of boundaries: The contact angle. Phys. Rev. E. 74: 651–657.

Chapman, S., and T.G. Cowling 1960. The mathematical Theory of Non-uniform Gases. Cambridge University Press, Cambridge.

Ghezzehei, T.A. 2004. Constrains for flow regimes on smooth fracture surfaces. Water Resour. Res. 40: Art. No. 03164.

Houseworth, J.E. 2006. An analytical model for solute transport in unsaturated flow through a single fracture and porous matrix. Water Resour. Res., 42: Art. No. 01416.

Huang, H., P. Meakin, M. Liu, and G.E. McCreery 2005. Modeling of multiphase fluid motion in fracture intersections and fracture networks. J. Geophys. Lett. 41:Art. No. 04204.

Inamuro, T., T. Ogata, S. Tajima, and N. Konishi 2004. A lattice-Boltzmann method for incompressible two-phase flows with large density differences. J. of Comp. Phys. 198: 626–644.

Lee, T., and C-L. Lin 2005. A stable discretization of the lattice Boltzmann equation for simulation of incompressible two-phase flow at high density ratio. J. Comp. Phys. 206:16–47.

Liu, H. -H., C. Doughty, and G.S. Bodvarsson 1998. An active fracture model for unsaturated flow and transport in fractured rocks. Water Resour. Res. 34:2633–2646.

Liu, H. -H., and G.S. Bodvarsson 2001. Constitutive relations for unsaturated flow in a fracture network. J. Hydrol. 252:116–125.

Liu, H. -H., C.F. Ahlers, G.S. Bodvarsson, A.L. Flint, and W.B. Guertal 2003. Modeling flow and transport in unsaturated fractured rock: an evaluation of continuum approach. J. Contam. Hydrol. 62–63:173–178.

Liu, H. -H., R. Salve, J.S. Wang, G.S. Bodvarsson, and D. Hudson 2004. Field investigation into unsaturated flow and transport in a fault: model analyses. J. Contam. Hydrol. 74:39–59.

Mathias, S.A., A.P. Butler, N. McIntyre, and H.S. Wheater 2005. The significance of flow in the matrix of Chalk unsaturated zone. J. Contam. Hydrol. 310:62–77.

Mongano, G.S., W.L. Singleton, T.C. Moyer, S.C. Beason, G.L.W. Eatman, A.L. Albin, and R.C. Lung 1999. Geology of the ECRB cross-drift-exploratory studies facility, Yucca Mountain project, Yucca Mountain, Nevada. SPG42GM3. LSN #: DEN001452480 Participant #: MOL.20000214.0134. U.S. Geological Survey, Denver, CO (http://www.lsnnet.gov/results.aspx).

Nieder-Westermann, G.H. 2000. Fracture geometry analysis for the stratigraphic units of the repository host horizon. ANL–EBS–GE–000006. Rev. 00. CRWMS M&O, Las Vegas, NV.

Pan, C., M. Hilpert, and C.T. Miller 2004. Lattice-Boltzmann simulation of two-phase flow in porous media. Water Resour. Res., 40: Art. No. W01501.

Qian, Y.H., D. D'Humieres, and P. Lallemand 1992. Lattice BGK models for Navier-Stokes equation. Europhys. Lett. 17:479–484.

Sbragaglia, M., and S. Succi 2006. A note on the lattice-Boltzmann method beyond the Chapman–Enskog limits. Europhys. Lett. 73:370–376.

Sbragaglia, M., R. Benzi, L. Biferale, S. Succi, and F. Toschi 2006. Surface roughness-hydrophobicity coupling in microchannel and nanochannel flows. Phys. Rev. Lett. 97:204503.

Sehgal, B.R., R.R. Nourgaliev, and T.N. Dinh 1999. Numerical simulation of droplet deformation and break-up by lattice-Boltzmann method. Progress in Nuclear Energy. 34:471–478.

Seol, Y., H. -H. Liu, and G.S. Bodvarsson 2003. Effects of dry fractures on matrix diffusion in unsaturated fractured rocks. Geophys. Res. Lett. 1029/2002GL016118.

Seol, Y., T.J. Kneafsey, and K. Ito 2006. An evaluation of the active fracture concept in modeling unsaturated flow and transport in fractured meter-sized block of rock. Vadose Zone J. 5:1–13.

Shan, X., and H. Chen 1993. Lattice Boltzmann model for simulating flows with multiple phases and components. Phys. Rev. E. 47:1815–1819.

Shan, X., and H. Chen 1994. Simulation of non-ideal gas phase transitions by the lattice Boltzmann equation. Phys. Rev. E. 49:2941–2948.

Shan, X., and G. Doolen 1995. Multicomponent lattice-Boltzmann model with interparticle interaction. J. Stat. Phys. 81: 379–393.

Smart, K.J., D.Y. Wyrick, P.S. Landis, and D.J. Waiting 2006. Summary and analysis of subsurface fracture data from the Topopah Spring Tuff upper lithophysal, middle nonlithophysal, lower lithophysal, and lower nonlithophysal zones at Yucca Mountain, Nevada. Center for Nuclear Waste Regulatory Analyses (CNWRA). LSN #: NRC000028356 Participant #: ML060660009. San Antonio, Texas. CNWRA 2005–04. (http://www.lsnnet.gov/results.aspx).

Su, F.W., J.T. Geller, K. Pruess, and F. Wen 1999. Experimental studies of water seepage and intermittent flow in unsaturated, rough-walled fractures. Water Resour. Res. 35:1019–1037.

Succi, S. 2001. The Lattice Boltzmann Equation for Fluid Dynamics and Beyond. Oxford University Press, Oxford.

Succi, S., E. Foti, and F. Higuera 1989. Simulation of three-dimensional flows in porous media with the lattice-Boltzmann method, Europhys. Lett. 10:433–438.

Sukop, M.C., and D. Or 2004. Lattice Boltzmann method for modeling liquid-vapor interface configurations in porous media. 40: Art. No. W01509.

Toschi, F., and S. Succi 2005. Lattice Boltzmann method at finite Knudsen numbers. Europhys. Lett. 69:549–555.

Wolf-Gadrow, D.A. 2000. A lattice Gas Cellular Automata and Lattice Boltzmann Model. Springer-Verlag, Berlin Heidelberg.

Wood, T.R., R.J. Glass, T.R. McJunkin, R.K. Podgorney, R.A. Laviolette, K.S. Noah, D.L. Stoner, R.C. Starr, and K. Baker 2004. Unsaturated flow through a small fracture-matrix network: Part 1. Experimental observations. Vadose Zone J. 3:90–100.

Yang, Z.L., T.N. Dinh, R.R. Nourgaliev, and B.R. Sehgal 2001. Numerical investigation of boiling regime transition mechanism by a lattice-Boltzmann model. Nuclear Engineering and Design. 204:143–153.

Zheng, H.W., C. Shu, and Y.T. Chew 2006). A lattice-Boltzmann model for multiphase flows with large density ration. J. of Comp. Phys. 218:353–371.

Zhou, Q., L.W. Gelhar, and B. Jacob 2002. Comparison of field-scale effective properties of two–phase flow in heterogeneous porous media obtained by stochastic analysis and numerical experiments. In: Findikakis, A.N. (Ed.), Proceedings of the International Groundwater Symposium on Bridging the Gap between Measurements and Modeling in Heterogeneous Media, Berkeley, California, March 25–29, 2002.

Zhou, Q., R. Salve, H. -H. Liu, J.S.Y. Wang, and D. Hudson 2006. Analysis of a mesoscale infiltration and water seepage test in unsaturated fractured rock: Spatial variabilities and discrete fracture patterns. J. Contam. Hydrol. 87:96–122.

List of Figures

Figure 1. (a) Flow domain geometry. Black represents no flow zones and gray represents flow channels; (b) flow channels were numbered as 5 horizontal channels and 14 vertical channels in (CS1); (c) each flow channel separated by a fracture junction was numbered separately (CS2). White circles in (c) mark the fracture junctions.

Figure 2. Lattice-Boltzmann simulation of injection of water into a channel network tilted by $2.5°$ in the counterclockwise direction. Snapshots were taken at (a) an early stage (t = 0.4ζ), (b) an intermediate stage (t = 0.8ζ), (c) a late stage (t = ζ), where ζ is the total simulation length. G_s = 0.22 (representing a wetting invading fluid); and G_f = -6.5 (corresponding to a density contrast of 70, which is the limit with the current SC potential). Gray represents the flow channels, black represents solid zones, and white represents the invading wetting fluid (water). The injection port is shown by a circle in the upper left side of the uppermost vertical channel.

Figure 3. Gravity-driven two-phase flow in a flow domain that consists of vertical and horizontal fractured channels. The flow domain was tilted counterclockwise at an angle (a) $0°$, (b) $1.5°$, (c) $4°$, (d) $12.5°$, (e) $13°$, (f) $20°$, (g) $35°$, and (h) $40°$. Simulations ended when the injected water reached the lower boundary.

Figure 4. Quasi-steady water saturations in tilted flow networks of Fig. 3.

Figure 5. Water saturation, S_f, and normalized solid-fluid interface, A'_{fm}/A_{fm}, as a function of the tilting angle of the apparatus. The reduced interface length is defined in reference to the maximum available solid-fluid interface length. Water saturations when the injected water reached the exit-end of the domain (a) and at the quasi-steady limit (b) were used.

Figure 6. Active fracture parameter, γ, as function of the fracture network orientation at two different arbitrarily chosen residual water saturation levels, S_r, using water saturations when the injected water reached the exit-end of the domain (Case 1) (a), and using quasi-steady water saturations (Case 2) (b).

Figure 7. Active fraction of fractures, f_a, at different fracture network orientations, θ, using water saturations when the injected water reached the exit-end of the domain (Case 1) (a) and using quasi-steady water saturations (Case 2) (b).

Figure 8. (a) Active fracture parameters, γ, computed by the fracture counting scheme in Fig. 1b (CS1) and in Fig. 1c (CS2), as a function of the fracture network orientation; (b) the correlation between γ for S_r =0.04 in Fig. 6 and γ obtained from two fracture counting schemes, N1 and N2.

Figure 9. Water (in white) was continuously injected into the flow domain at a constant rate from (a) one, (b) two, (c) four, and (d) eight equally spaced injection ports. Black dots in the uppermost vertical channel represent the location of injection ports. The flow domain was tilted $2.5°$ counterclockwise.

Figure 10. Temporal variations in (a) water saturation; (b) ratio of active solid-fluid interface length to the maximum available solid-fluid interface length; (c) active fracture model parameter, γ; and (d) active fraction of fractures, f_a. S_r was set to 0.04.

Figure 11. Temporal variations in (a) water saturation; (b) ratio of active solid-fluid interface to the maximum potentially available solid-fluid interface, A'_{fm}/A_{fm}; (c) active fracture model parameter, γ; and (d) active fraction of fractures, f_a, as a function of normalized injection intervals (normalized by the total simulation length for which water was injected into the domain without interruption).

Figure 12. Water (in white) was injected into the flow domain at a constant rate from a single injection port at an interval of (a) 0.04, (b) 0.25, (c) 0.33, and (d) 0.72. The injection intervals in Fig. 11 were normalized by the total simulation length for which water was injected into the domain without interruption. The flow domain was slanted counterclockwise by $2.5°$. S_r was set to 0.04.
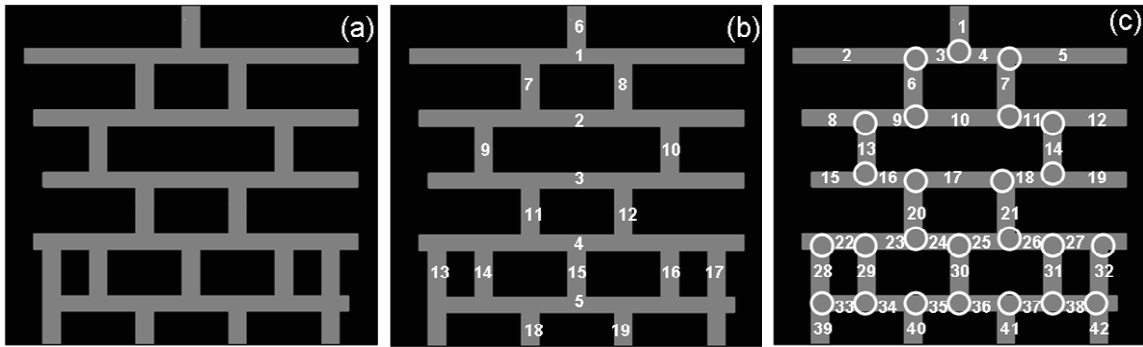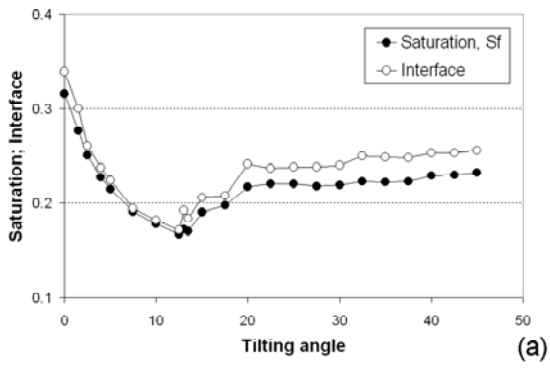
Figure 1
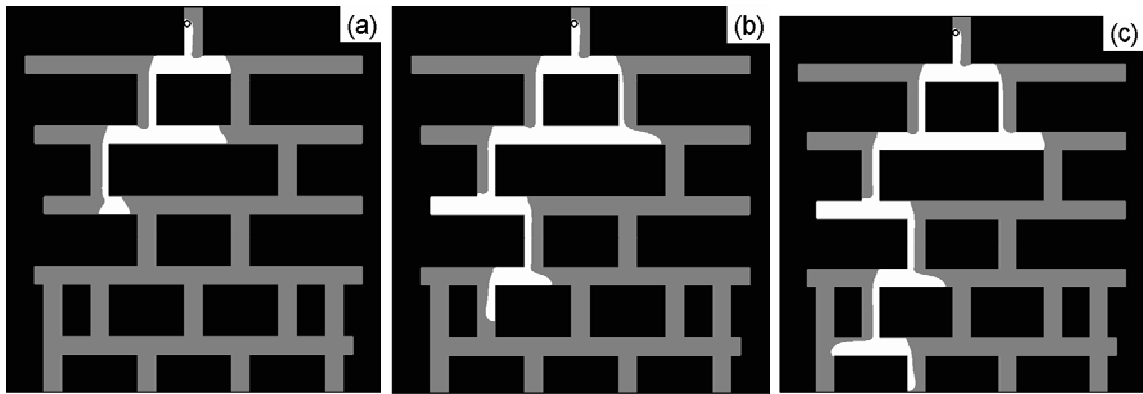
Figure 2
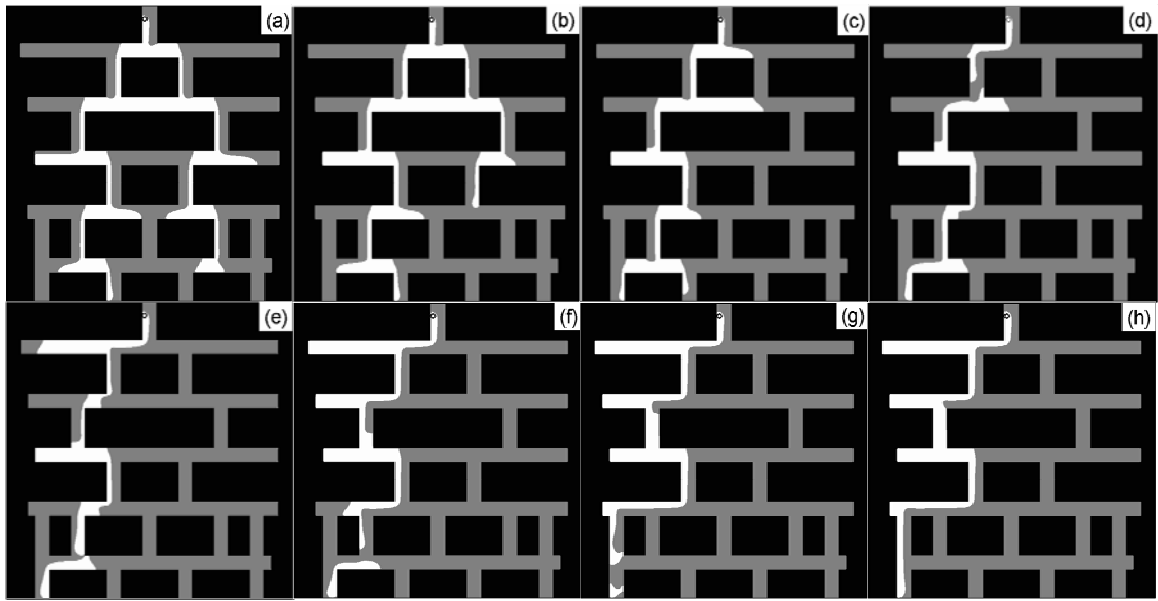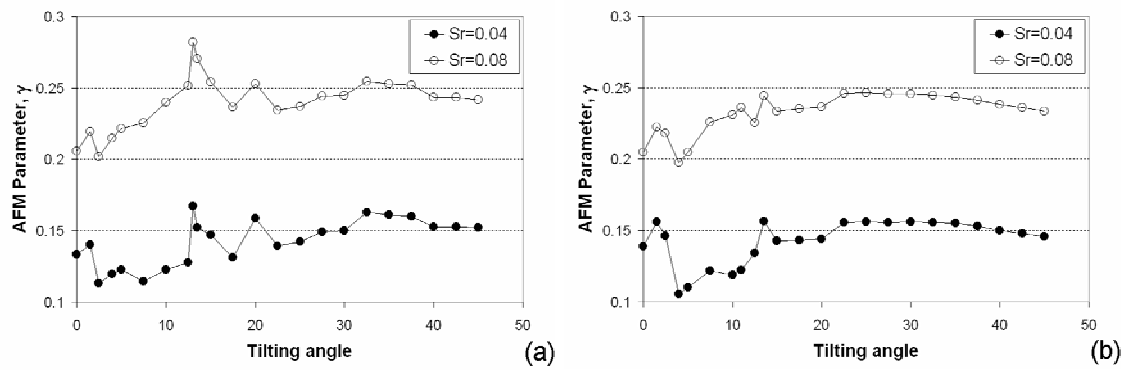
Figure 3
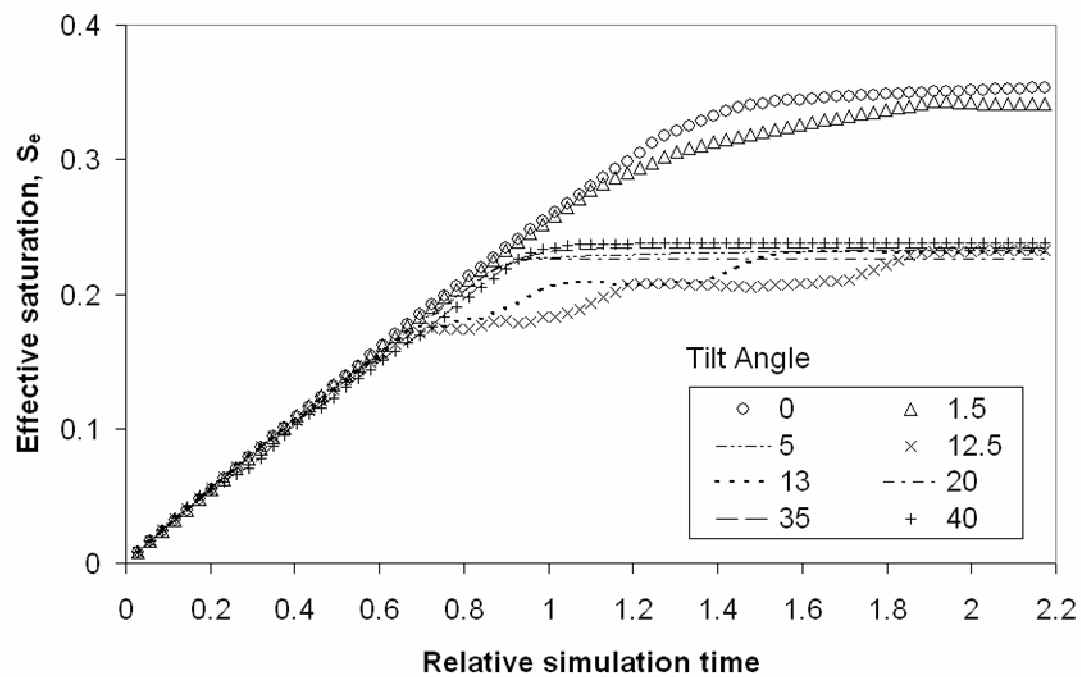
Figure 4
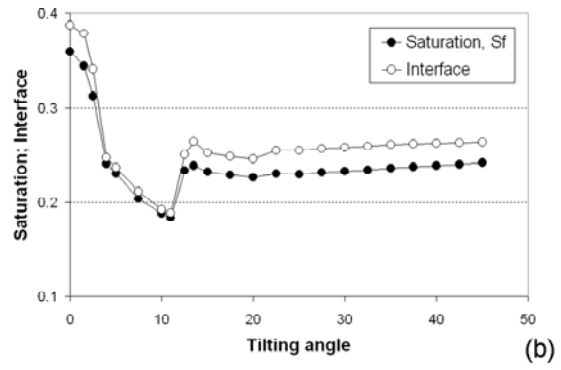
Figure 5

Figure 6

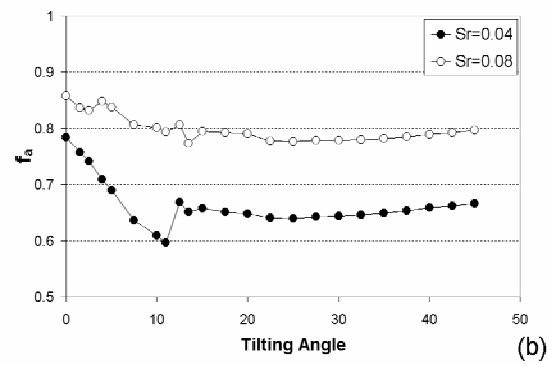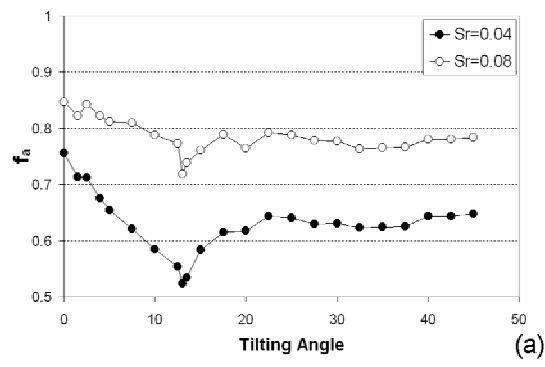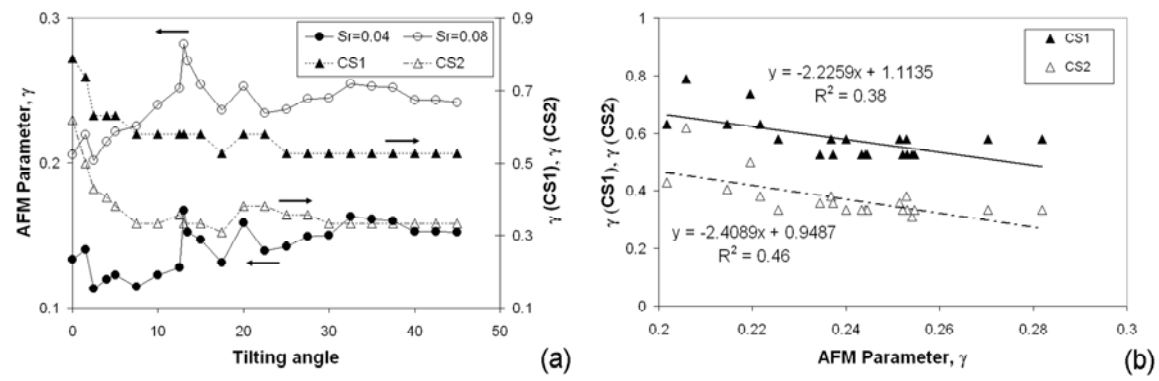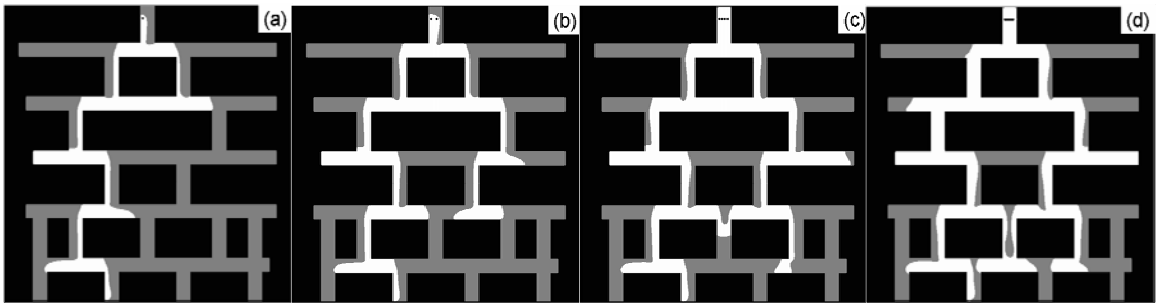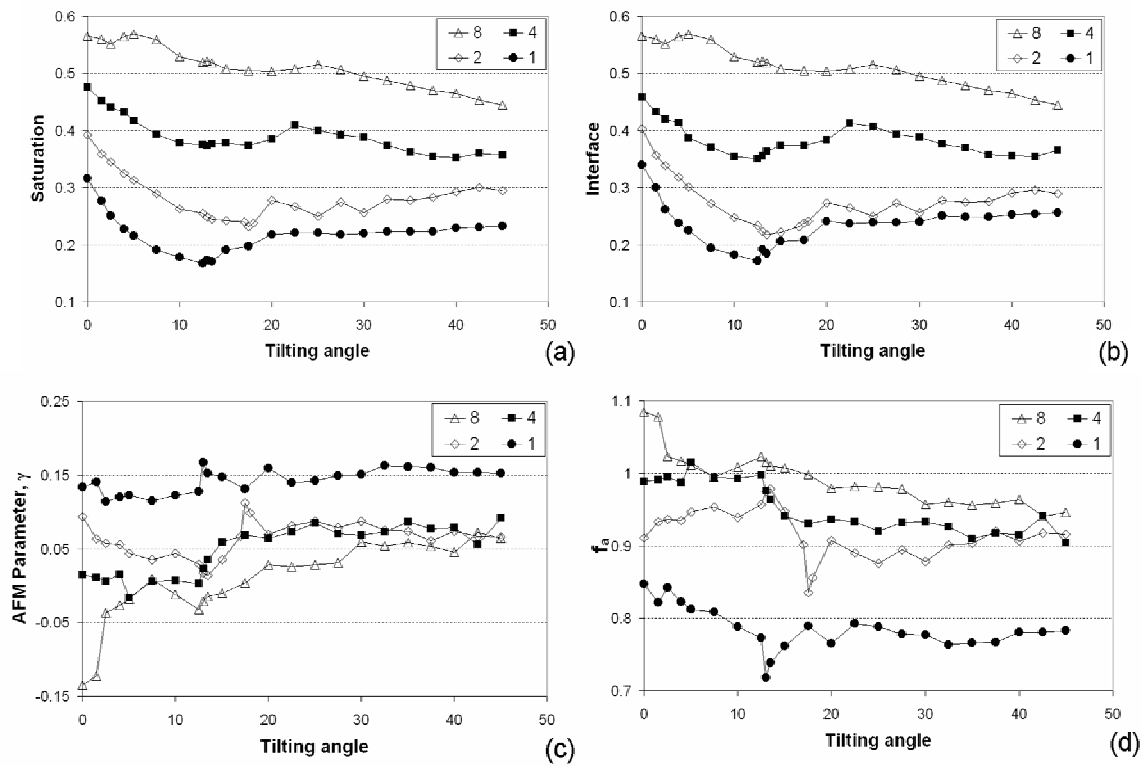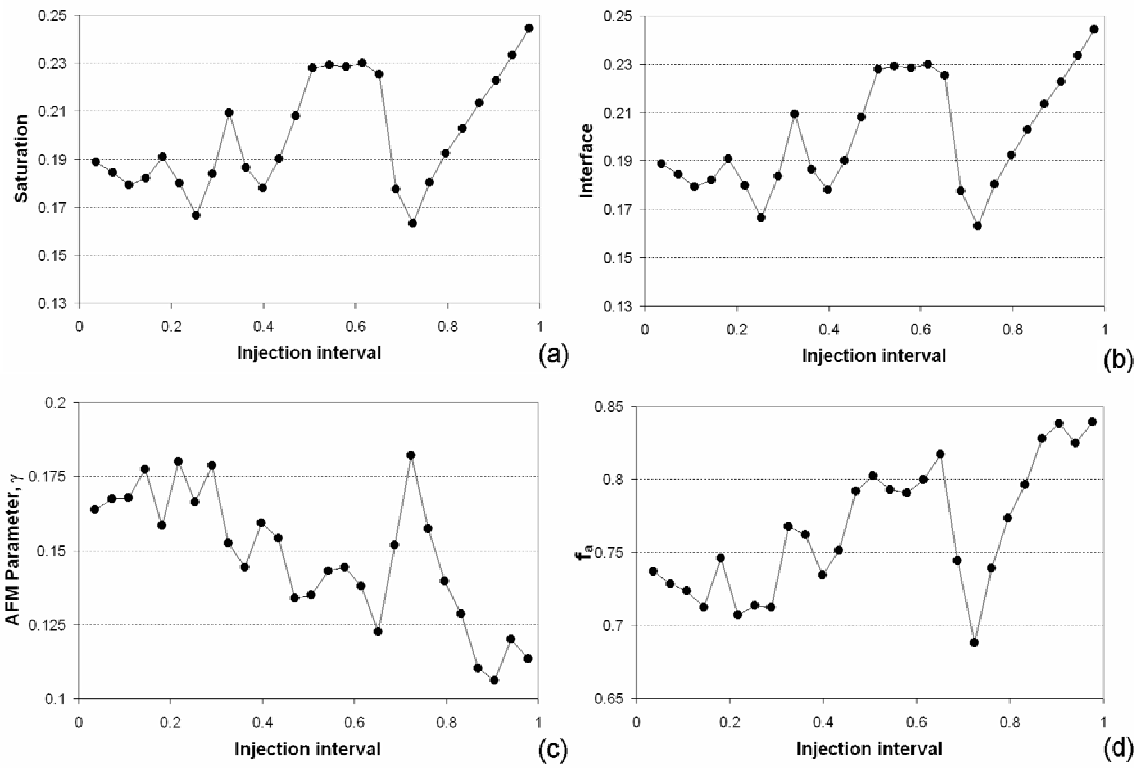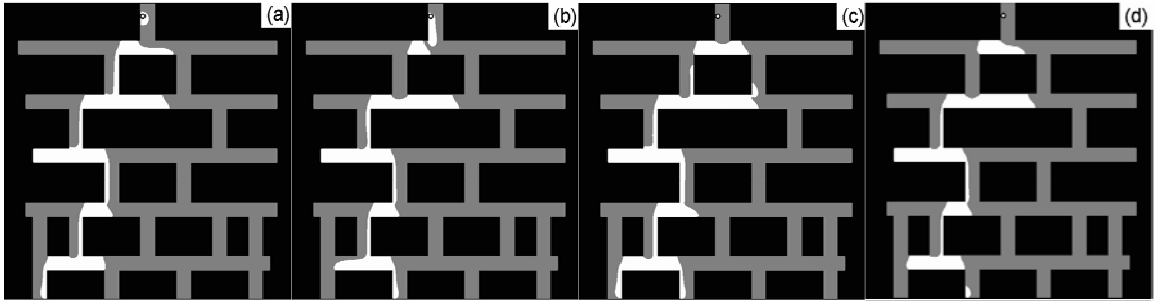**Figure 7**

Figure 8

Figure 9

Figure 10

Figure 11

Figure 12